

# Developing an Explainable Variational Autoencoder (VAE) Framework for Accurate Representation of Local Circulation in Taiwan

Min-Ken Hsieh<sup>1</sup> and Chien-Ming Wu<sup>1</sup>

<sup>1</sup>National Taiwan University

November 14, 2023

## Abstract

This study develops an explainable variational autoencoder (VAE) framework to efficiently generate high-fidelity local circulation patterns in Taiwan, ensuring an accurate representation of the physical relationship between generated local circulation and upstream synoptic flow regimes. Large ensemble semi-realistic simulations were conducted using a high-resolution (2 km) model, TaiwanVVM, where critical characteristics of various synoptic flow regimes were carefully selected to focus on the effects of local circulation variations. The VAE was constructed to capture essential representations of local circulation scenarios associated with the lee vortices by training on the ensemble dataset. The VAE's latent space effectively captures the synoptic flow regimes as controlling factors, aligning with the physical understanding of Taiwan's local circulation dynamics. The critical transition of flow regimes under the influence of southeasterly synoptic flow regimes is also well represented in the VAE's latent space. This indicates that the VAE can learn the nonlinear characteristics of the multiscale interactions involving the lee vortex. The latent space within VAE can serve as a reduced-order model for predicting local circulation using synoptic wind speed and direction. This explainable VAE ensures the accurate predictions of the nonlinear characteristics of multiscale interactions between synoptic flows and the local circulation induced by topography, thereby accelerating the assessments under various climate change scenarios.

## Hosted file

978609\_0\_art\_file\_11573907\_s3gd5g.docx available at <https://authorea.com/users/673236/articles/685974-developing-an-explainable-variational-autoencoder-vae-framework-for-accurate-representation-of-local-circulation-in-taiwan>

1  
2  
3  
4  
5  
6  
7  
8  
9  
10  
11  
12  
13  
14

## **Developing an Explainable Variational Autoencoder (VAE) Framework for Accurate Representation of Local Circulation in Taiwan**

**Min-Ken Hsieh<sup>1</sup> and Chien-Ming Wu<sup>1</sup>**

<sup>1</sup> Department of Atmospheric Sciences, National Taiwan University, Taipei, Taiwan

Corresponding author: Chien-Ming Wu ([mog@as.ntu.edu.tw](mailto:mog@as.ntu.edu.tw))

### **Key Points:**

- An Explainable artificial intelligence is constructed to capture Taiwan’s local circulation using TaiwanVVM ensemble simulations.
- The representation of local circulation in the latent space of the VAE can be formulated as synoptic wind speed and direction.
- This framework can effectively generate accurate local circulation in Taiwan for fast climate response assessment.

## 15 **Abstract**

16 This study develops an explainable variational autoencoder (VAE) framework to efficiently  
17 generate high-fidelity local circulation patterns in Taiwan, ensuring an accurate representation of  
18 the physical relationship between generated local circulation and upstream synoptic flow  
19 regimes. Large ensemble semi-realistic simulations were conducted using a high-resolution (2  
20 km) model, TaiwanVVM, where critical characteristics of various synoptic flow regimes were  
21 carefully selected to focus on the effects of local circulation variations. The VAE was  
22 constructed to capture essential representations of local circulation scenarios associated with the  
23 lee vortices by training on the ensemble dataset. The VAE's latent space effectively captures the  
24 synoptic flow regimes as controlling factors, aligning with the physical understanding of  
25 Taiwan's local circulation dynamics. The critical transition of flow regimes under the influence  
26 of southeasterly synoptic flow regimes is also well represented in the VAE's latent space. This  
27 indicates that the VAE can learn the nonlinear characteristics of the multiscale interactions  
28 involving the lee vortex. The latent space within VAE can serve as a reduced-order model for  
29 predicting local circulation using synoptic wind speed and direction. This explainable VAE  
30 ensures the accurate predictions of the nonlinear characteristics of multiscale interactions  
31 between synoptic flows and the local circulation induced by topography, thereby accelerating the  
32 assessments under various climate change scenarios.

33

## 34 **Plain Language Summary**

35 This research introduces an advanced neural network framework for generating high-  
36 fidelity local flow patterns in Taiwan. This framework, known as an explainable variational  
37 autoencoder, can accurately simulate how wind patterns of synoptic weather conditions interact  
38 in this region. We used detailed simulations to train the variational autoencoder, ensuring it  
39 captures the complex relationships between local flow and larger-scale weather patterns. By  
40 training on the detailed simulations, the variational autoencoder learned and represented these  
41 large-scale weather patterns in a way that helps maintain the physical relationship between local  
42 flow prediction and the large-scale weather patterns. One of the key outcomes of this study is the  
43 development of a reduced-order model. This simplified model takes advantage of what we have  
44 learned about complex weather interactions and can quickly predict local weather under different  
45 conditions. This approach ensures accurate predictions, even in complex situations involving  
46 changing climate conditions.

## 47 **1 Introduction**

48 The advances in data-driven Artificial intelligence (AI) /Deep Learning (DL) models for  
49 weather forecasting (e.g. Pangu-Weather (Bi et al., 2023), FourCastNet (Pathak et al., 2022) and  
50 GraphCast (Lam et al., 2022)) that significantly lower computational cost, offering a promising  
51 alternative to state-of-the-art numerical weather prediction (NWP) models. As the frequency and  
52 intensity of extreme weather events increase in the warming earth, deep generative models have  
53 garnered significant interest in meeting the demand for accurately assessing the intensity, timing,  
54 and spatial distribution of local extreme weather events, with a particular focus on generative  
55 adversarial networks (GANs) (Goodfellow et al., 2014). The applications of GANs are mostly  
56 gaining traction in the realm of extreme precipitation, such as estimating single-site precipitation  
57 patterns (Zadrozny et al., 2021), generating extreme precipitation (Bhatia et al., 2020),

58 reconstructing missing information in microwave precipitation data (Wang et al., 2021), and  
59 generating spatiotemporal weather patterns of extreme events (Klemmer et al., 2021). These  
60 research efforts exemplify the potential of deep generative models in addressing the challenges  
61 associated with extreme weather events and signify a promising direction for enhancing weather  
62 forecasting capabilities.

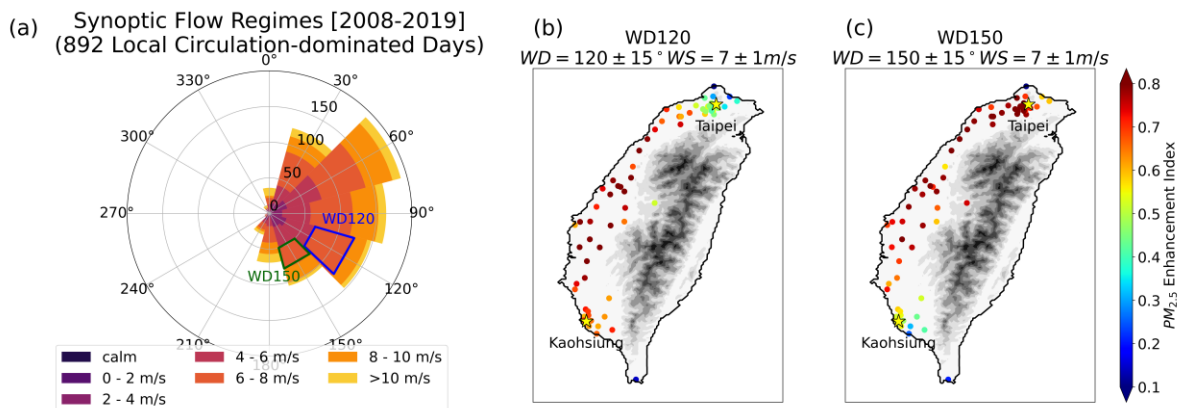
63 As an alternative, Variational Autoencoders (VAEs) (Kingma & Welling, 2014; 2019,  
64 hereafter KW2019) offer an encoder-decoder generative model that explicitly learns the  
65 distribution of the training set. By regularizing the latent space to a known distribution, VAEs  
66 enable stochastic synthesis that is primarily controlled by the latent space distribution. This  
67 allows researchers to identify where to sample from to achieve synthesis with specific desired  
68 characteristics. This property enhances the interpretability of VAE-based generative models.  
69 VAE applications have showcased their effectiveness in discussing weather fields in extreme  
70 scenarios, as demonstrated by Oliveira et al. (2021) and Behrens et al. (2022). Their results show  
71 that VAEs can skillfully reproduce subgrid cloud processes and reveal key cloud-type features.  
72 In addition, Shamekh et al. (2022) showed improved estimations of precipitation variability  
73 using VAE-learned low-dimensional variables for convection aggregation at the subgrid scale.

74 While deep generative models show progress in efficiently exploring the physics of  
75 geosciences, there remains a significant concern. Purely data-driven DL models might  
76 sometimes lack consistency in their predictions concerning established laws of physics (Daw et  
77 al., 2017). Additionally, the limited number of labeled instances available for training or cross-  
78 validation can often fail to accurately represent the underlying relationships in scientific  
79 problems (Karpatne et al., 2017). This concern becomes even more pronounced when applying  
80 DL models trained with current climate data to infer scenarios in a warming climate. The  
81 changing conditions and unique characteristics of a warming climate can lead to uncertainties  
82 and challenges in model generalization, raising questions about the reliability and robustness of  
83 data-driven approaches in such contexts.

84 The recent emergence of physics-informed neural networks (PINNs) has provided a  
85 promising approach to addressing the challenges of purely data-driven DL models. In a  
86 pioneering study, Beucler et al. (2021) introduced a climate-invariant machine learning approach  
87 that involves transforming the input/output features of the DL framework into a set of physical  
88 parameters with consistent distributions across different climates. Their findings demonstrated  
89 that incorporating physical considerations, even in the data preprocessing stage, can enhance the  
90 performance of DL models. This highlights the potential for bridging the gap between DL  
91 models and physics knowledge, thereby imposing physical constraints on model outputs and  
92 improving prediction skills for unseen scenarios.

93 In this study, we aim to utilize the neural network to address the evaluation of the local  
94 circulation induced by complex topography, which remains one of the most challenging aspects  
95 in global general circulation models (GCMs), even under sub-hundred-kilometer resolutions.  
96 Consequently, evaluating local responses to climate change often relies heavily on dynamical  
97 downscaling approaches. These approaches perform high-resolution numerical simulations to  
98 acquire detailed information on local phenomena under specific warming scenarios. However,  
99 the dynamical downscaling approach demands substantial computation resources and can  
100 introduce uncertainties, leading to the "cascade of uncertainty" in assessing the local responses to  
101 the various climate projections (Wilby and Dessai, 2010).

102 Taiwan provides a natural laboratory for studying AI downscaling where complex  
 103 orography is generally underrepresented in current models even at kilometer scales. With nearly  
 104 200 summits surpassing 3000 m within its central mountain range, covering two-thirds of its  
 105 total 36000 km<sup>2</sup> area, the island's complex topography interacts with large-scale synoptic  
 106 conditions to induce a diverse array of local circulations. These local circulations control various  
 107 weather phenomena, such as air pollution transport, which is well discussed in the literature (Lai  
 108 and Lin, 2020; Hsieh et al., 2022, hereafter H2022; Hsu et al., 2023, hereafter H2023). These  
 109 studies suggested that the local circulation can be dramatically different under the slight change  
 110 of the synoptic flow regimes, and consequently impacts the air pollution scenarios in Taiwan.  
 111 Figure 1 depicts the local pollution patterns as an indicator of the local circulation scenarios to  
 112 demonstrate the impacts of the synoptic flow regime change on the local flow patterns. By  
 113 carefully selecting local-circulation dominated days, which exclude the impact of long-range  
 114 pollutant transport by cyclones, cold surges, and strong northeasterly winds in the highly-  
 115 polluted cold season (Oct. to Apr.), the windrose in Fig. 1a reveals the variation of synoptic near-  
 116 surface flow regimes near Taiwan (the average wind direction and speed below 925 hPa in the  
 117 sounding data at Ishigaki island, Japan). We select the southeasterly flow regimes with a slight  
 118 change in wind direction (wind direction veers from 120° to 150°) to display the PM<sub>2.5</sub> pollution  
 119 scenarios bifurcation as shown in Fig. 1b and Fig. 1c, named as WD120 and WD150 flow  
 120 regimes respectively. For each distinct flow regime, we chose cases where the synoptic wind  
 121 directions fell within a 30-degree range and the wind speeds were limited to a 2 m s<sup>-1</sup> range (as  
 122 shown in the titles of Fig. 1b and 1c). The dots over Taiwan in Fig. 1b and 1c are color-coded  
 123 based on the enhancement index, which considers the historical frequency of observed aerosol  
 124 concentration exceeding the 12-year average that can exclude the effects of uneven local  
 125 emissions as suggested by H2023. Figure 1b (1c) shows that the PM<sub>2.5</sub> pollution deteriorates over  
 126 the south (north) Taiwan around Kaohsiung (Taipei) while the pollution on the north (south)  
 127 corner near Taipei (Kaohsiung) is alleviated. The contrast between Fig. 1b and Fig. 1c  
 128 demonstrates that the local pollution scenarios can be significantly changed by only a 30°  
 129 shifting of the synoptic prevailing wind direction. Despite the aforementioned studies confirming  
 130 that local circulation plays a crucial role in linking large-scale flow regimes to local pollution  
 131 patterns, obtaining detailed information about local circulation requires computationally  
 132 intensive physical numerical models, as shown in a case study by Lin et al. (2022).



133  
 134 **Fig 1. The local pollution scenarios controlled by the synoptic flow regimes. (a) The**  
 135 **frequency distribution of synoptic flow regimes in the local circulation-dominated days in**  
 136 **the cold season (Oct. to Apr.) from 2008 to 2019. (b) The PM<sub>2.5</sub> pollution enhancement**  
 137 **index under WD120 synoptic flow regimes indicated by the blue bracket in subfigure (a).**

138 **(c) The  $PM_{2.5}$  pollution enhancement index under WD150 synoptic flow regimes indicated**  
139 **by the green bracket in subfigure (a). The yellow asterisks in (b) and (c) indicate Taipei and**  
140 **Kaohsiung city, Taiwan's major cities.**

141

142 In this study, we propose the generation of local circulation using an explainable VAE  
143 framework trained by the large ensemble dataset from the numerical simulation focusing on the  
144 specific pollution weather regime as mentioned above. The physically constrained training  
145 dataset allows the VAE to learn the nonlinear physical relationship between the local circulation  
146 and the upstream synoptic flow regimes. To capture the multiscale interaction between synoptic  
147 conditions and local circulations over complex terrain, we employ the high-resolution physics  
148 model, TaiwanVVM (Wu et al. 2019, hereafter W2019), to generate a physically constrained  
149 dataset. Leveraging the semi-realistic TaiwanVVM simulation framework, we conduct an  
150 ensemble of simulations to generate detailed local circulation scenarios under various synoptic  
151 forcing regimes in observations. The ensemble of high-dimensional simulations serves as an  
152 analogy of the large-eddy-simulation library driven by large-scale forcing that expands the  
153 dataset in various synoptic regimes available for DL approaches learning from (Shen et al.,  
154 2022).

155 By employing this dataset, a VAE model is trained ensuring that the model learns  
156 physically consistent solutions. We show that the 2-dimensional latent space of the VAE well  
157 captures the variability of the local circulations associated with the lee vortices in the training  
158 data, and the trained VAE can generate realistic local circulations. The manifold provided by  
159 VAE is further interpreted as the physical parameters of upstream flow regimes that drive the  
160 variability of the local flows in the training data, which is aligned with understanding of the  
161 leeside local circulation formation mechanism. Consequently, in conjunction with the decoder,  
162 the physically-interpreted manifold can function as a reduced-order model that can generate the  
163 high-fidelity local circulation induced by the topography of Taiwan with high efficiency.

164 Our approach emphasizes that VAE can learn fluid dynamics through training on a large  
165 ensemble of LES that captures the large-scale variability of the controlling factors on a specific  
166 fluid phenomenon, such as the leeside flow structure in this study. Given the large-scale  
167 conditions, the reduced-order model derived from the VAE can predict high-resolution local  
168 circulation under various climate change scenarios. To demonstrate the capability of this  
169 framework, we apply the reduced order model to downscale the crucial synoptic flow pattern  
170 change at the end of the century in the climate projection from a member of Coupled Model  
171 Intercomparison Project Phase 6 (CMIP6, Eyring et al., 2017), namely Taiwan Earth System  
172 Model Version 1(TaiESM1, Lee et al., 2020). The generated local circulations provide a physical  
173 fundamental to predict the potential pollution deterioration in the major cities of Taiwan. The  
174 manuscript is organized as follows. The TaiwanVVM semi-realistic ensemble dataset and the  
175 construction of the explainable VAE framework are described in section 2. The results and their  
176 physical interpretation are depicted in section 3, followed by the application of the reduced-order  
177 model and discussion in section 4.

178 **2 Data and Methods**179 **2.1 Semi-Realistic TaiwanVVM Simulation Dataset**

180 To incorporate physical consistent data as the training dataset of the VAE  
 181 framework, we employ a physical model known as TaiwanVVM (W2019) to generate  
 182 physics-constrained training data. TaiwanVVM is a simulation framework based on the  
 183 Vector Vorticity equation cloud-resolving Model (VVM, Jung and Arakawa, 2008),  
 184 featuring a realistic representation of Taiwan's topography using the immersed boundary  
 185 method (Wu and Arakawa, 2011; Chien and Wu, 2016). This model has been extensively  
 186 utilized in studies concerning local precipitation hotspots (Kuo and Wu, 2019; Chang et  
 187 al., 2021, hereafter C2021). A series of studies focused on the local pollution distribution  
 188 scenarios also suggested that the TaiwanVVM model can evaluate the variability of the  
 189 lee vortices flow patterns under various synoptic prevailing wind conditions (H2022;  
 190 H2023). These studies have demonstrated the model's capability to capture  
 191 comprehensive information about the local circulation and highlighted its reliability and  
 192 suitability for generating physics-constrained training data for the VAE framework. The  
 193 TaiwanVVM framework details are presented in Table 1. The simulation starts at 6:00  
 194 local time with a 24-hour duration so that the diurnal local flows induced by the heating  
 195 difference over the complex topography can develop and further interact with the large-  
 196 scale prevailing winds. The overall simulation setup follows H2022 while relaxing the  
 197 horizontal and vertical resolution to enlarge the simulation domain that better covers the  
 198 entire lee side local circulations while remaining to resolve the crucial flow structures we  
 199 focus on.

200

201 **Table 1. TaiwanVVM simulation framework**

Horizontal Resolution	2 km
Vertical Resolution	46 m near surface and stretch up to 969 m at model top
Land Surface Model	Noah Land Surface Model version 3.4.1 coupled with land type and topography of Taiwan (Wu et al., 2019)
Representation of topography	Immersed boundary method with block mountain in height coordinate (Wu and Arakawa 2011; Chien and Wu 2016)
Lateral Boundary Condition	Double periodic

202

203

204

205

206

207

208

209

To generate realistic local circulations under various synoptic conditions using VAE, it is essential to introduce the variability of synoptic conditions into the simulation of the physics model. To address this, we adopt a semi-realistic simulation framework proposed in C2021, employing sounding observations as uniform initial conditions across the entire domain. This approach emphasizes the influence of controlling environmental factors that govern the development of local circulations. We utilize sounding observations from Ishigaki Island, Japan, to represent the synoptic conditions in the semi-

210 realistic simulations. Figure 1a illustrates the variability of synoptic flow regimes on days  
211 dominated by local circulation, showing that prevailing winds are primarily confined to  
212 northeasterly and southeasterly directions. This observation aligns with the assumption  
213 that Ishigaki Island is located upstream of Taiwan. Subsequently, we extend the selection  
214 of local circulation-dominated days from 1980 to 2020, subjectively choosing 197 out of  
215 a total of 2893 days to conduct the large ensemble TaiwanVVM simulations. By  
216 incorporating the variability of the synoptic environment, our semi-realistic simulation  
217 framework accounts for the diverse local circulations resulting from the interaction  
218 between synoptic forcing and the physical effects of topography, including diurnal  
219 heating differences and the blocking of prevailing flow. This physics-constrained  
220 ensemble dataset is then prepared for representation learning using the VAE.

## 221 2.2 Variational Autoencoder

222 Autoencoder (AE) is a specific neural network architecture distinguished by its  
223 unique bottleneck structure. This feature endows AEs with the capability of performing  
224 effective nonlinear dimension reduction, making it a valuable tool in geoscience  
225 applications that often seek the crucial features or coherent structures within patterns in  
226 considerable volumes of data. Operating as an unsupervised representation learning  
227 framework, AEs excel at extracting the essential hidden manifold that optimally captures  
228 the variability present in the input data. However, the pitfall of AEs is that the latent  
229 space is constrained solely by the reconstruction loss. Minimizing reconstruction error  
230 tends to obtain an overfitting AE, in which fair reconstruction results are accompanied by  
231 the latent space that is only partially defined and incomplete. The gaps between the points  
232 representing the training data in the latent space are undefined, which means that the  
233 manifold is not continuous and does not allow interpolation, leading to the incapability of  
234 physical interpretation. The VAE proposed by KW2019 offers a solution to the challenge  
235 of unregulated latent spaces within AEs while also introducing generative capabilities  
236 across the entire space. The VAE's encoder generates parameters for a predefined  
237 distribution within the latent space. Subsequently, the VAE enforces a constraint on this  
238 latent distribution to adhere to a normal distribution. A brief description of VAE  
239 following KW2019 is provided below.

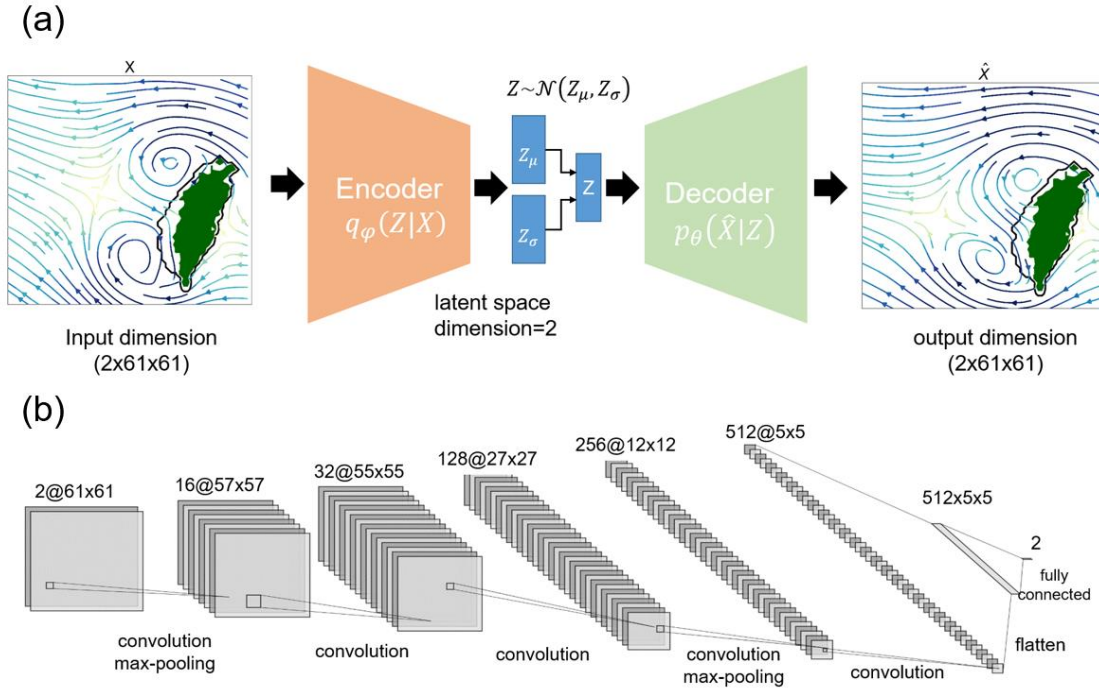


**Fig. 2 The convolutional variational autoencoder framework. (a) The schematics of variational autoencoder framework. (b) The design of the convolutional encoder.**

To replace the deterministic latent variables employed in AEs with latent distributions, as illustrated in Fig. 2a, the encoder within the VAE is conceptualized as a probabilistic encoder. Its primary function involves estimating the posterior probability of latent vectors  $Z$  given observed input  $X$  and parameterized by  $\theta$ , denoted as  $p_\theta(Z|X)$ . However, as pointed out by KW2019,  $p_\theta(Z|X)$  is usually intractable or excessively intricate. Consequently, the encoder functions as an inference model, aiming to identify a surrogate distribution,  $q_\phi(Z|X)$ , that effectively approximates the posterior of these intricate latent distributions parameterized by  $\phi$ . Thus, to achieve this approximation, the Gaussian distribution is commonly chosen as the form for the approximate posterior distribution. By leveraging encoder-derived parameters for mean  $Z_\mu$  and variance  $Z_\sigma$  the approximate posterior distribution  $\mathcal{N}(Z_\mu, Z_\sigma)$  is formulated. By introducing the Kullback-Leibler (KL) divergence, a quantification of the closeness between two distributions, we can gauge the dissimilarity between our normal distribution characterized by parameters  $Z_\mu$  and  $Z_\sigma$ , and the prior distribution. Notably, as discussed by KW2019, the calculation of the KL divergence possesses a closed-form expression when assuming the standard Gaussian distribution  $\mathcal{N}(0,1)$  as the prior distribution:

$$D_{KL}[\mathcal{N}(Z_\mu, Z_\sigma) || \mathcal{N}(0,1)] = -0.5 \sum_{i=1}^N 1 + \log(Z_{\sigma_i}^2) - Z_{\mu_i}^2 - Z_{\sigma_i}^2 \quad (1)$$

In Equation (1), the summation encompasses all  $N$  dimensions within the latent space. Utilizing the logarithm of variance in computing the KL divergence is preferred to facilitate an output range comprising natural numbers rather than solely positive values. This choice promotes smoother representations of the latent space. Including the KL

266 divergence within the VAE's loss function bestows it with a regularization role, ensuring  
 267 alignment of the latent distribution with a normal distribution. Consequently, this  
 268 enforces a more structured and well-controlled depiction of the latent space.

269 Within the VAE framework, as visually depicted in Fig. 2a, the latent variable  
 270 vector  $Z$  is sampled from the latent distribution. This distribution is parameterized by the  
 271 mean and standard deviation outputted from the encoder. Subsequently, the latent  
 272 variable vector  $Z$  is input into the decoder to generate the desired output. This stochastic  
 273 sampling procedure can be described as follows:

$$274 \quad Z \sim \mathcal{N}(Z_\mu, Z_\sigma) \quad (2)$$

275 In the gradient-based training procedure of VAE, the loss derived from the  
 276 outputs necessitates backward propagation across the entire network for parameter  
 277 refinement. However, this random sampling process creates a bottleneck as gradients  
 278 cannot effectively propagate through the sampling layer. Consequently, this limitation  
 279 impedes the learning of parameters  $Z_\mu$  and  $Z_\sigma$ . To address this challenge, KW2019  
 280 devised a reparameterization trick, which reformulates Equation (2) as follows:

$$281 \quad \begin{aligned} Z &= \mu + \sigma \odot \epsilon \\ \epsilon &\sim \mathcal{N}(0,1) \end{aligned} \quad (3)$$

282 In Equation (3) the  $\odot$  donates elementwise multiplication and the latent variable  
 283 vector  $Z$  is calculated by a fixed mean  $Z_\mu$  plus the fixed standard deviation  $Z_\sigma$  scaled by a  
 284 random sampled  $\epsilon$  from unit Gaussian distribution. This rearrangement achieves the same  
 285 outcome as the random sampling process described in Equation (2). Importantly, this  
 286 reparameterization converts the calculating of  $Z$ , involving  $Z_\mu$  and  $Z_\sigma$ , into deterministic  
 287 nodes. Consequently, this adjustment enables the seamless passage of gradients, ensuring  
 288 effective gradient backpropagation throughout the network.

289 As the reparameterization trick adopted to preserve the stochasticity in the  
 290 decoder and the KL divergence in Equation (1) introduced as a regularization loss,  
 291 KW2019 successfully showcased the feasibility of constructing a VAE framework. This  
 292 framework enables the establishment of a continuous end-to-end training process aimed  
 293 at extracting the latent distribution from the given data. Within the context of this study,  
 294 the loss function for the VAE is formulated as follows:

$$295 \quad loss_{VAE} = loss_{reconstruction} + \beta loss_{regularization}$$

$$296 \quad = \sum_{x \in X} \|x - \hat{x}\| + \beta D_{KL}[\mathcal{N}(Z_\mu, Z_\sigma) || \mathcal{N}(0, I)] \quad (4)$$

297 The first term in Equation (4) is reconstruction loss, aiming to attain high-quality  
 298 reconstruction akin to the loss definition in the conventional AE. The reconstruction loss  
 299 assesses the fidelity of the reconstructed data, where  $x$  represents a sample, and  $\hat{x}$   
 300 represents its corresponding reconstruction. The second term corresponds to the KL  
 301 divergence penalty, serving to regularize the latent space, as elaborated earlier. In order to  
 302 achieve an optimal equilibrium between the precise reconstruction of the input data and  
 303 the acquisition of meaningful representations within the latent space, we introduced a  
 304 parameter  $\beta$  governing the weighting applied to the regularization loss. By incorporating  
 305 Equation (1) and opting for the mean square difference as the reconstruction loss metric,  
 306 we can formulate Equation (4) as follows:

$$307 \quad loss_{VAE} = \frac{1}{M} \sum_{k=1}^M (x_k - \hat{x}_k)^2 + \beta (-0.5 \sum_{i=1}^N 1 + \log(Z_{\sigma_i}^2) - Z_{\mu_i}^2 - Z_{\sigma_i}^2) \quad (5)$$

308 In Equation (5),  $M$  refers to the amount of the training samples and  $N$  represents  
309 the latent dimensions. By minimizing this loss metric during the training process, the  
310 regularized latent distribution can be taken as a complete and continuous representation  
311 of the variability in the training dataset with only  $N$  dimensions. It is always desired to  
312 gain a representation of the variability in atmospheric data with only a few dimensions  
313 since the spatial-temporal variations of atmospheric phenomena are usually displayed by  
314 data with hundreds or thousands of dimensions. The complete and continuous  
315 representation can also be elaborated in a more physical sense. Moreover, the VAE as a  
316 generative model can generate new high-dimensional data by sampling the learned latent  
317 distribution. This functionality creates an opportunity for constructing a reduced-order  
318 model for predicting local circulation with high efficiency. In the next subsection, we  
319 elaborate on the construction of the explainable VAE framework that binds the semi-  
320 realistic ensemble simulations to the VAE.

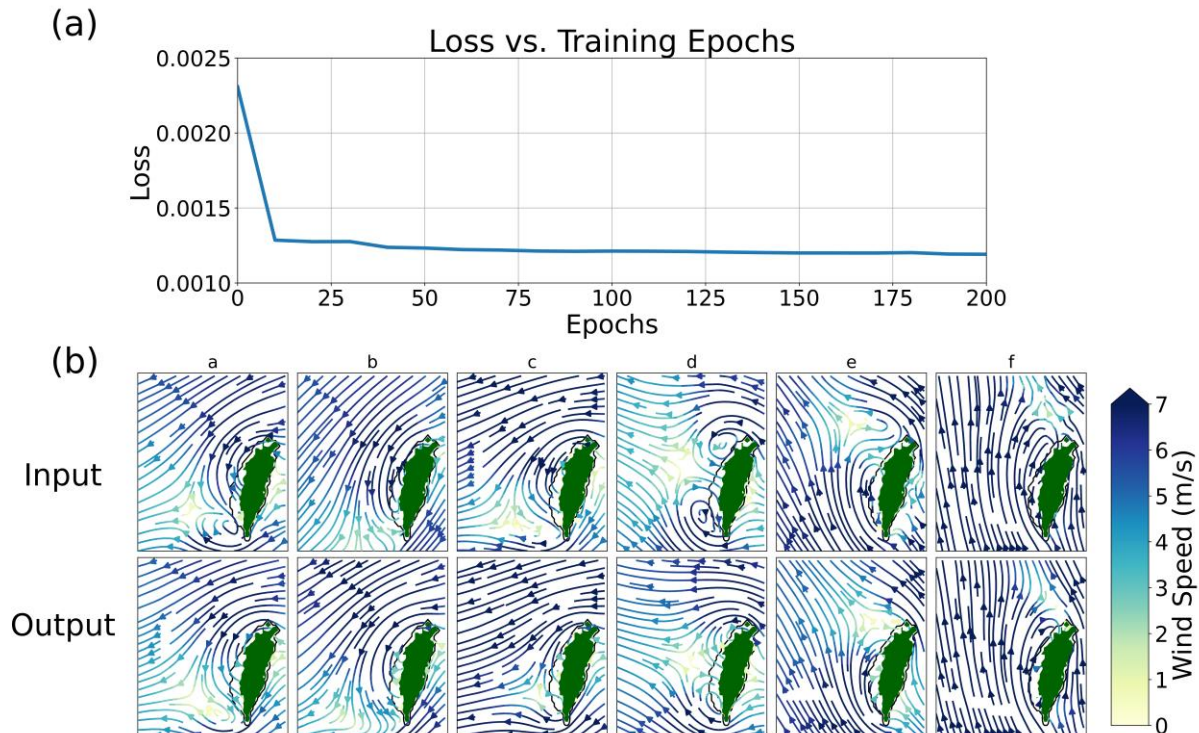
### 321 2.3 Explainable VAE Framework

322 In this study, we aim to construct a DL generative model that can physically  
323 evaluate the local circulation of Taiwan. While the idealized tracer transport simulation  
324 study confirmed that the synoptic prevailing flow regime is crucial in controlling the  
325 local circulation patterns of Taiwan (H2022), the nonlinear critical transition of the local  
326 circulation scenarios under the synoptic conditions in the real world, as depicted in Fig. 1,  
327 still needs further evaluation. We conducted the semi-realistic TaiwanVVM ensemble  
328 simulations as depicted in 2.1 to encompass the variability of the local circulation  
329 scenarios under various synoptic conditions. By taking the ensemble dataset as the  
330 training data, we incorporate the underlying physics from the TaiwanVVM model into  
331 the representation learning process of the VAE.

332 From a total of 197 simulations, we collected output wind field snapshots within  
333 an 18-hour span starting from 8:00 local time with a 20-minute frequency as the VAE  
334 training data. This selection enables the inclusion of the local circulation's diurnal  
335 evolution while excluding the first two hours for model spinning-up. The snapshot of  
336 simulated 3-dimensional wind fields is a massive volume, making it a challenge as a  
337 single training example. To address this issue, we strategically focused on the near-  
338 surface horizontal winds at the lowest level over the west plain of Taiwan in the  
339 simulation (160 m above sea level) as a surrogate of the local circulations. These  
340 horizontal wind fields exhibit distinct scenarios under various synoptic flow regimes. To  
341 further manage the data size, we trimmed the horizontal spans of the 2-dimensional wind  
342 fields to a subspace of the entire domain and downsampled them to a 10-km resolution  
343 where the wake of the prevailing synoptic flow is present. The 10-km resolution  
344 horizontal wind field from the ensemble simulation results serves as the training data for  
345 the VAE. This dataset comprises  $u$ -wind and  $v$ -wind components in a  $61 \times 61$  horizontal  
346 grid with a total of 9456 samples for the representation learning in VAE as displayed in  
347 Fig. 2.

348 Utilizing a dataset comprising 9456 physically constrained samples, we construct  
349 the encoder and decoder of the VAE employing five convolutional layers. The  
350 convolutional architecture of the encoder is displayed in Fig. 2b, while the decoder is the  
351 reverse setup with deconvolution layers. The convolutional layers are designed to  
352 effectively capture spatial features inherent in the local circulation patterns present within

353 the training data. The hyperbolic tangent function was employed as the activation  
 354 function across all layers, ensuring the output of each layer is confined within -1 to 1. By  
 355 testing the effects of the scaling parameter of the regularization KL divergence  $\beta$  in  
 356 Equation (5), we found that the VAE cannot reconstruct the various input local  
 357 circulations when  $\beta$  exceeds 0.2. We select the  $\beta$  as 0.1 to gain the fair reconstruction  
 358 under a mild regularization. For the choice of latent dimension  $N$ , a 3-dimensional latent  
 359 space of AE shows that most of the projected points of the training data are gathered on a  
 360 plane, indicating that a 2-dimensional latent space is sufficient to capture the variability  
 361 of the training samples. As a result, we set the latent dimensions  $N$  as 2 to conduct the  
 362 training procedure. We used the Adam optimizer with a learning rate of 0.001, We  
 363 trained the models for 1000 epochs. All experiments were carried out using Nvidia  
 364 GP100 GPUs.



365 **Fig. 3** The training results of the VAE. (a) The decrease of loss in the training process in the  
 366 first 200 epochs. (b) The comparison of local circulations reconstructed by VAE and the  
 367 original input data in 6 samples. The local circulations are displayed as the streamlines,  
 368 and the color represents the wind speed (m/s). The green shading area indicates the  
 369 mountain areas of Taiwan where the ground level is above 200 m. The upper row displays  
 370 the input training data in these 6 samples, the corresponding reconstruction outputs are  
 371 shown in the same column of the lower row.

372  
 373  
 374 The training results are summarized in Fig. 3. Figure 3a illustrates the progressive  
 375 decrease of the total loss in the first 200 epochs of the training procedure. These training  
 376 iterations exhibit an initial rapid reduction of the loss within the first 100 epochs,  
 377 followed by a slight decline to levels below 0.0012 with fluctuations to the end of  
 378 training. By meticulously minimizing the loss, the VAE undergoes training to accurately  
 379 reconstruct diverse local circulation training samples, as shown in Fig. 3b. The subfigure

380 columns, ranging from “a” to “f” in Fig. 3b, showcase distinct local flow patterns  
381 corresponding to the shifting synoptic flow regimes. As the prevailing wind direction  
382 changes from northeasterly to southeasterly, the local flow structure over Taiwan’s  
383 western region undergoes a transition from a pronounced northerly pattern with a reverse  
384 flow located at the southwest of Taiwan (column “a” in Fig. 3b) to a dipole configuration  
385 of lee vortices (column “d” in Fig. 3b), and ultimately to a more prominent southerly  
386 accompanied with the reverse flow near northern Taiwan scenario (column “f” in Fig. 3b).  
387 This sequence of evolving scenarios highlights the dynamic multiscale interaction  
388 between synoptic conditions and local flow patterns. Importantly, the training samples  
389 (the upper row of Fig. 3b) distinctly display the flow structure of lee vortices with these  
390 varying scenarios, affirming the effectiveness of our training data extraction methodology  
391 in addressing the challenge of high-dimensional data, while successfully preserving the  
392 fundamental attributes of the local circulation patterns as derived from the physical model.

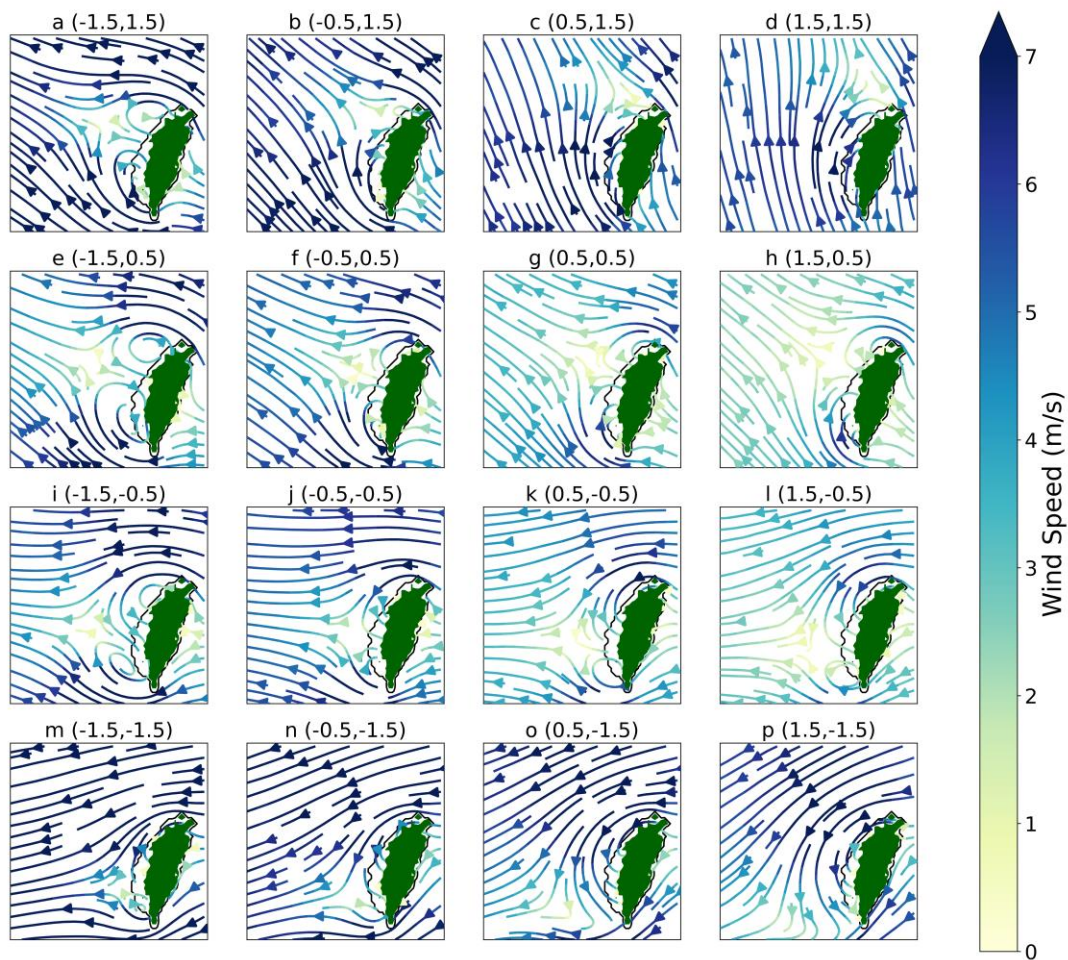
393 In addition, the comparison between input samples (the upper row of Fig. 3b) and  
394 their corresponding reconstructed local circulations (the lower row of Fig. 3b) indicates  
395 that the VAE adeptly encompasses the coherent structures of the local circulations which  
396 are presented within the input data. Given that the core attributes of the local circulation  
397 remain intact in the reconstruction outputs, it can be inferred that the latent space derived  
398 from the VAE captures the essential representation of the local circulation. Notably, the  
399 assessment of the reconstruction also underscores the distinctive aspect of the VAE as a  
400 deep generative model. While other deep generative models such as GAN can produce a  
401 synthetic output through the random sampling process, their sampling distribution often  
402 comprises pre-defined Gaussian noise that is irrelevant to the generating performance.  
403 For example, the training process of GAN is reinforced through the competition between  
404 the discriminator and generator, yielding improved results while incapable of exploring  
405 the hidden structures of the training data. In contrast, VAEs are explicitly designed to  
406 uncover hidden manifolds through the training data. The success of reconstruction can be  
407 attributed to the VAE’s ability to capture the training samples via latent distributions. To  
408 explore the capability of VAE to infer the physical meaning of the training data, we  
409 inspect the latent space of the trained VAE in the next section.

### 410 **3 Results**

411 As the VAE is capable of reconstructing realistic local circulations akin to the input data,  
412 we further examine the robustness of the VAE by inspecting the various local circulations  
413 generated from the latent space. As 88.5% of the latent vectors of the training data are gathered  
414 within the  $x \in [-2, 2], y \in [-2, 2]$  subspace in the latent space, we focus on this area of latent space for  
415 further examination. By evenly sampling this subspace, we generate a matrix of the local  
416 circulation as displayed in Fig. 4. The sampling locations in the latent space are indicated in the  
417 titles of subfigures in Fig. 4. The entire local circulation matrix shows the continuous variations  
418 of the various local circulations, which is attributed to the normal distribution of the latent  
419 vectors regularized in VAE. As the latent vectors sampling locations near the left edge of the  
420  $x \in [-2, 2], y \in [-2, 2]$  subspace (Figs. 4a, e, i, m), the decoder can generate distinct local circulation  
421 associated with the lee vortices accompanied by different prevailing flows from southeasterly to  
422 northeasterly. For example, the generative local flow from point  $(x=-1.5, y=1.5)$  of the latent  
423 space shows that the signature of the local flow under the prevailing southeasterly is the presence  
424 of circular flow patterns associated with lee vortices in the wake of mountains and the

425 acceleration zones on the rear of the north and south capes of the topography (Fig. 4a). As the  
 426 sampling point moves toward the lower left corner ( $x=-1.5, y=-1.5$ ) of the latent space, the  
 427 generating local flows turn into a profound northeasterly with lee vortex circulation located on  
 428 the southwest of Taiwan (Fig. 4m). Furthermore, upon comparing the upper row (Figs. 4a to 4d)  
 429 with the lower row (Figs. 4m to 4p) of the local circulation array, it becomes evident that the  
 430 local circulations in the lower row exhibit a notably consistent pattern, while the upper row  
 431 displays a distinct transition. This transition manifests as a shift from a dipole pattern of lee  
 432 vortices under prevailing southeasterly conditions (Fig. 4a) to a milder anti-cyclonic curved flow  
 433 pattern in a southerly environment (Fig. 4d). These findings illustrate that the generation process,  
 434 using evenly sampled locations in the latent space, can effectively reproduce the nonlinear  
 435 transitions observed in local circulations.

### Generated Local Circulation



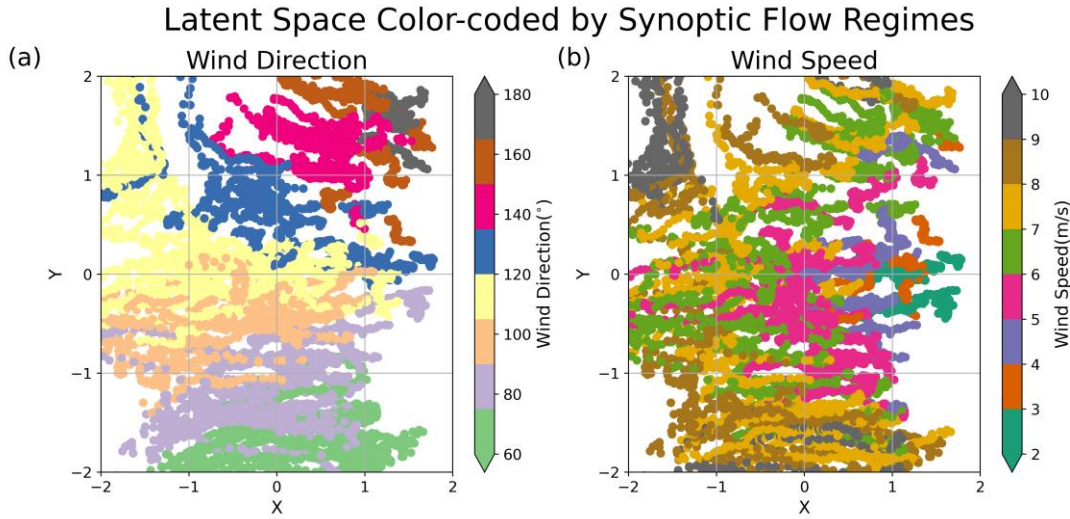
436 **Fig. 4** The local circulations generated by evenly sampling the latent space. The sampling  
 437 points of the latent space are titled in the subfigures.  
 438  
 439

440 Examining the variability in the generated local flows suggests that the VAE can produce  
441 reasonable local circulations under various specific prevailing winds. The essential low-  
442 dimensional latent distributions well capture the change in the prevailing flow regimes and the  
443 subsequent local circulations. It implies that the variability in local flows corresponding to  
444 different flow regimes embedded in the training data has been learned by the VAE through the  
445 training process. As we constrain the training data as the semi-realistic ensemble simulation  
446 results, the ensemble spread could be crucial clues for interpreting the latent space. In the  
447 TaiwanVVM simulation procedures, we prescribed the sounding observations as the initial  
448 conditions in the selected 197 local circulation-dominated cases to conduct the semi-realistic  
449 ensemble simulations. We take the near-surface (below 925 hPa) prevailing mean wind speeds  
450 and directions as the physical parameters of these simulations to discuss the physical implication  
451 of the latent space since the variability of the local circulations is controlled by the synoptic low-  
452 level flow regimes, as evidenced by the idealized simulations in H2022. The latent vectors of the  
453 training samples color-coded by the physical flow regimes are displayed in Fig. 5. The latent  
454 vectors spanned in the two-dimensional latent space, after being colored by corresponding initial  
455 synoptic wind speeds and directions of individual semi-realistic simulations, demonstrate that the  
456 lower-dimensional representations of the various local circulations are generally associated to  
457 their synoptic flow regimes. The latent vectors of the training samples induced by the synoptic  
458 southerly (darker colors in Fig. 5a) are projected in the upper right corner of the latent space, as  
459 shown in Fig. 5a. The lower half of the latent space is clustered of the latent vectors that  
460 represent the local circulations under the prevailing synoptic northerly to northeasterly (from 20°  
461 to 80° roughly) in the TaiwanVVM simulations. The training samples of the local circulations  
462 associated with the easterly synoptic winds occupy the middle and left parts of the latent space.  
463 As the various synoptic wind directions can be identified in the latent space, Fig. 5b also displays  
464 that the latent vectors resulting from different synoptic wind speeds are clearly separated., The  
465 latent vectors in the area of  $x \in [1, 2]$ ,  $y \in [-0.5, 0.5]$  are compressed from the local circulations  
466 induced by weak wind conditions (synoptic wind speed is less than  $4 \text{ m s}^{-1}$ ), whereas the latent  
467 vectors projected to the upper-right or lower-right corner represent the local circulations in the  
468 simulations of stronger synoptic wind conditions.

469 The results show that different characteristics of the prescribed synoptic winds of the  
470 simulations are separated in the latent space of VAE, highlighting the role of synoptic variability  
471 on the local circulations. The shift in the latent space could be depicted as the gradual changes in  
472 synoptic flow regimes. We take advantage of the VAE that constrains the latent space as a  
473 continuous space to depict the variability of the local circulation in the semi-realistic ensemble  
474 dataset. As the various responses of the local circulation scenarios controlled by the different  
475 synoptic controlling factors are captured in the semi-realistic ensemble simulations, the VAE  
476 successfully learned this physical representation of the variability of local circulations in Taiwan  
477 and consequently secures the transparency of this framework through the interpretable latent  
478 space.

479 Within the physically-interpreted latent space, it is worth noting that the sharp transition  
480 of the generated local circulations, as shown in the top row of Fig. 4, can be attributed to the  
481 synoptic southeasterly flow regime, which is displayed as the dots near the top boundary with  
482 darker colors in Fig. 5. The sharp transition of the generated local circulations (Figs. 4a to 4d) by  
483 moving the sampling point from point  $(x=-1.5, y=1.5)$  to point  $(x=1.5, y=1.5)$  in the latent space  
484 can be elaborated as the shifting of the synoptic prevailing wind direction from about 120° to  
485 160°. It shows that the VAE learned from the semi-realistic ensemble simulation dataset is

486 capable of generating a critical transition of local circulations under the gradual varying of the  
 487 synoptic flow regimes.



488  
 489 **Fig. 5 The latent vectors of the training samples color-coded by (a) the synoptic wind**  
 490 **directions and (b) the synoptic wind speeds.**  
 491

492 As we constrain the training dataset of VAE through the physical simulations with the  
 493 semi-realistic experiment design focusing on the topographically induced local circulation of  
 494 Taiwan, the nonlinear compression functionality of the VAE can greatly reduce the complexity  
 495 of multiscale interaction phenomena in atmospheric fluid dynamics. The resulting latent space  
 496 with physical meaning, along with the decoder as a generative model, can serve as a reduced-  
 497 order model that elaborates the pattern of the local circulation under a specific synoptic flow  
 498 regime. To achieve this goal, we quantify the distribution of the representative synoptic flow  
 499 regimes in the latent space using linear interpolation and simple least square curve fitting. The  
 500 selection of fitting function forms is inspired by the visualization of the interpolated parameters  
 501 in the latent space, as shown in Fig. 5. As the wind speeds of the latent vectors are distributed  
 502 radially, and the wind directions vary along the y-axis, we select the elliptical and linear  
 503 forms to transform the orthogonal coordinates of latent space to the synoptic wind speed and  
 504 direction, as follows:

$$505 \quad WD = a + b \tan^{-1}\left(\frac{cy}{x-d}\right) \quad (6)$$

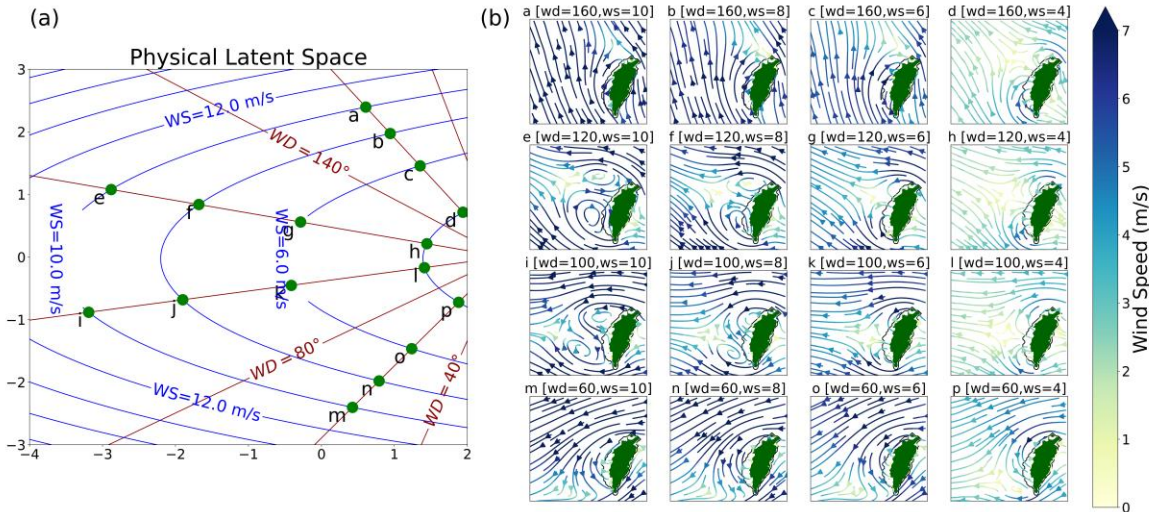
$$506 \quad WS = a(x - \alpha)^2 + b(y - \beta)^2 \quad (7)$$

507 where  $x$  and  $y$  denote the cartesian coordinates of the 2-dimensional latent space, and  $a$ ,  $b$ ,  
 508  $c$ ,  $d$  in Equation (6), and  $a$ ,  $b$ ,  $\alpha$ ,  $\beta$  in Equation (7) are the fitting parameters.

509 Figure 6a illustrates the contours of the fitting functions of synoptic wind directions and  
 510 speeds within  $x \in [-2, 4]$ ,  $y \in [-3, 3]$  subspace in the latent space (details of the fitting parameters are  
 511 depicted in the figure captions of Fig. 6a). With the mean absolute errors of the transformation  
 512 confined to  $0.71 \text{ m s}^{-1}$  in wind speed and  $5.76^\circ$  in wind direction, the 2-dimensional latent space  
 513 is spanned by synoptic flow regimes. The weak wind regime is located near the center of the  
 514 right boundary, while the strong wind flow regimes are distributed toward the other boundaries.  
 515 The synoptic northerly/northeasterly regimes occupy the lower half of the latent space, and the  
 516 southeasterly/southerly synoptic flows can be identified on the upper half of the plane. While  
 517 higher-order fitting functions can minimize fitting errors, we aim to demonstrate the capability of

518 the VAE to transform the latent space into physical parameters-based coordinates while  
 519 maintaining the simplicity of the entire framework. Through this transformation, the new  
 520 coordinates of the latent space can fulfill the alignment with the variability in the training  
 521 samples represented by the latent vectors and offer a physical explanation of the latent  
 522 distributions that can generate the high-fidelity local circulations.

#### Various Generated Local Circulations Corresponding to Synoptic Flow Regime Change



523 **Fig. 6 (a) The contours of the synoptic wind direction (red lines) and wind speed (blue lines)**  
 524 **derived by the fitting functions. The fitting function forms are selected as Equation (6) and**  
 525 **Equation (7), where the fitting parameters for the wind direction fitting function are**  
 526  **$a=118.7$ ,  $b=0.99$ ,  $c=1$ ,  $d=2.5$ , and the parameters are  $a=0.05$ ,  $b=0.89$ ,  $\alpha=10.06$ ,  $\beta=0.02$  for the**  
 527 **wind speed. (b) the generated high-fidelity local circulations. The local circulations**  
 528 **correspond to the sampling points (green dots in subfigure (a)) in the latent space are**  
 529 **shown in the titles of subfigures in (b) along with the synoptic wind directions and speeds.**  
 530

531

532 By taking the latent space as a synoptic flow regime phase diagram, we construct the  
 533 matrix of generated local circulations corresponding to the gradual changes in the synoptic flow  
 534 regimes, as shown in Fig. 6b. The sampled locations in the latent space are selected as specific  
 535 synoptic flow regimes that veer from southeasterly (on the upper half of the latent space) to  
 536 northeasterly (on the lower half of the latent space), as well as the intensification of the  
 537 prevailing wind speed (moves along the red lines in Fig. 6a from the central area near the right  
 538 boundary to other boundaries radially). The corresponding variability of local circulations in the  
 539 matrix (Fig. 6b) displays the reasonable scenarios in lee vortex flow structures. Upon examining  
 540 the variation among the rows of the local circulation matrix, we can identify the impact of  
 541 changes in wind direction. Notably, prevailing easterly winds tend to result in a dipole structure  
 542 of the lee vortices on the west plain of Taiwan (Fig 6b-h and 6b-l). Moreover, when the  
 543 prevailing wind direction shifts to southerly (northerly), it promotes the formation of cyclonic  
 544 (anti-cyclonic) lee vortices, as evident in Fig. 6b-d (Fig. 6b-p). In addition, the effects of changes  
 545 in synoptic wind speed are demonstrated through the local circulations across different columns  
 of the matrix. Instances of the lee vortices stalling near the topography can be observed in Fig.

547 6b-h and 6b-g; the lee vortices tend to be shedding away from the topography as the prevailing  
548 winds intensified, as shown in Fig. 6b-f and 6b-e.

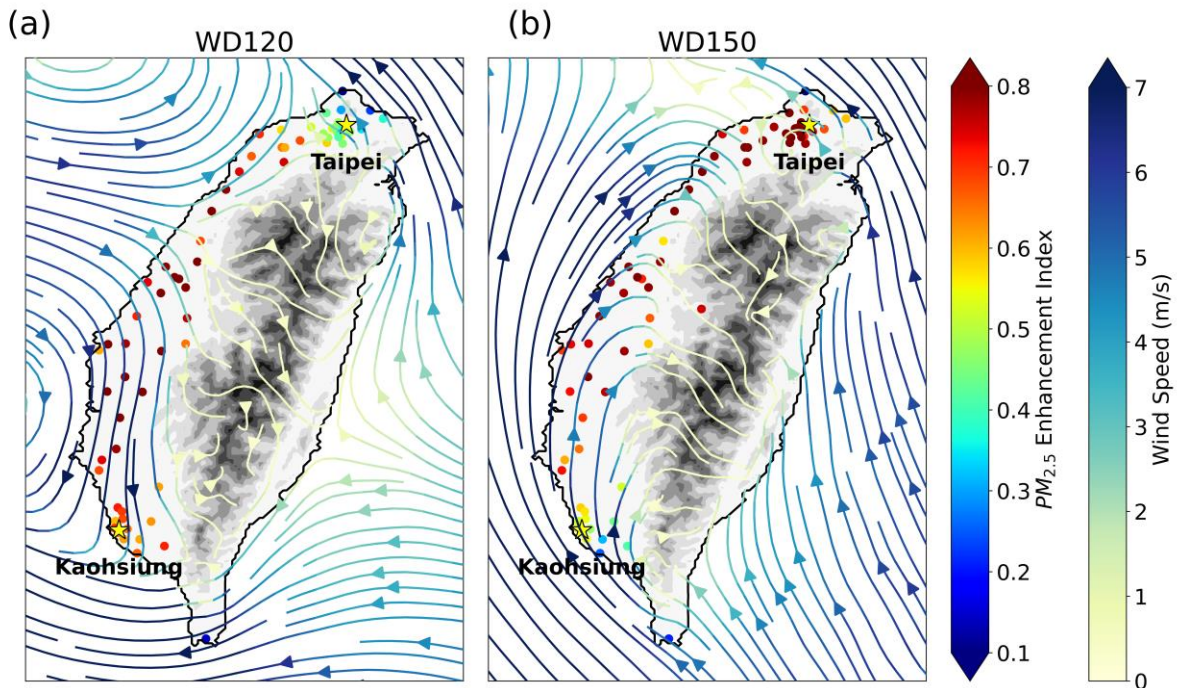
549 The compelling outcomes of the VAE serve as a valuable reduced-order model capable  
550 of generating local circulation from specific synoptic flow regimes, thereby conserving  
551 computational resources compared to the integration of traditional physics models. This  
552 approach showcases the potential of VAE as an effective AI downscaling tool for advancing our  
553 evaluation of complex local circulation under various climate change scenarios in the warming  
554 climate, in which the physics fundamental and the explainability are utmost essential demands.

#### 555 **4 Applicaiton and Discussion**

556 In this study, we employed the VAE to learn the physical mechanism of the vortex  
557 formation of Taiwan in the semi-realistic TaiwanVVM simulations. The selection of suitable  
558 synoptic environments and the subsequent physics model simulation procedures served as  
559 essential physical preprocessing steps for the machine learning framework. The VAE excels in  
560 nonlinear dimension reduction of high-dimensional dynamic fields in the atmospheric domain,  
561 allowing us to extract essential features from the complex atmospheric data. Meanwhile, the  
562 TaiwanVVM simulation results adhere rigorously to physical laws and provide a robust  
563 foundation for the VAE to learn the physical representations of the variability in the local  
564 circulations in Taiwan. Through this integration of machine learning and physics-based  
565 simulations, we gained valuable high-fidelity local circulation through the VAE that can be  
566 explained physically.

567 As the VAE takes these physically constrained training data to learn from and further  
568 create a continuous phase diagram that can elaborate the variability in the training samples in  
569 terms of the synoptic conditions of the ensemble simulations, the VAE has yielded a reduced-  
570 order model capable of producing realistic and high-fidelity local circulation patterns in response  
571 to specific synoptic flow regimes. To demonstrate the application of the reduced-order model in  
572 examining the local weather, we revisit the PM<sub>2.5</sub> deterioration scenarios shown in Fig.1.

## Generated Local Circulation using VAE



573 **Fig. 7 (a) The generated local circulation (streamlines) and the observed local pollution**  
 574 **enhancement index (colored dots) in Taiwan in the selected WD120 flow regime as depicted**  
 575 **in Fig. 1a). (b) Same as (a) but in the selected WD150 flow regime. The PM<sub>2.5</sub> enhancement**  
 576 **index and the definition of the WD120/WD150 are the same as depicted in Fig. 1b and 1c.**  
 577 **The local circulations are generated from the reduced-order model derived from the VAE**  
 578 **with the average synoptic wind speeds and directions of the selected days within**  
 579 **WD120/WD150 are projected into the latent space.**  
 580

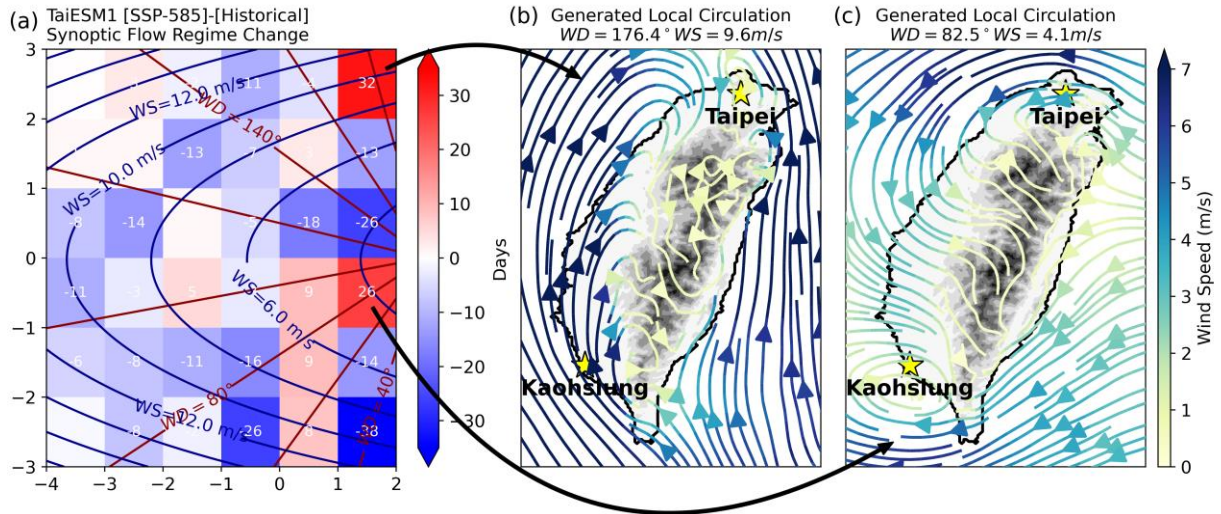
581  
 582 As depicted in the introduction section, the bifurcation of the local PM<sub>2.5</sub> pollution  
 583 enhancement scenarios implies a distinct change in local circulations between WD120 and  
 584 WD150 synoptic flow regimes. By projecting the selected cases' mean wind direction and speed  
 585 into the latent space of the VAE, the local circulations corresponding to WD120 and WD150  
 586 flow regimes can be generated using this reduced-order model. Figure 7 displays the generated  
 587 local circulations along with the PM<sub>2.5</sub> enhancement indices under WD120 and WD150 flow  
 588 regimes, as revealed in Fig. 1. The high-fidelity local circulations provide insights into the  
 589 underlying pollutants transport processes that are responsible for the distinct local pollution  
 590 deterioration. As displayed in Fig. 7a, a dipole of the lee vortices is identified in the local  
 591 circulation under the WD120 flow regime. The local circulation over northern Taiwan is  
 592 dominated by the cyclonic flow of the lee vortex located on the northern Taiwan Strait. On the  
 593 other hand, the northerly on the central and south areas of the west plain of Taiwan can be  
 594 attributed to the anti-cyclonic circulation of the other vortex located on the southern Taiwan  
 595 Strait. As the major local emission sites are located on the west coastline of central and southern  
 596 Taiwan, the local circulation on the west plain of Taiwan in Fig. 7a promotes the transport of the  
 597 local pollutants both northward and southward, resulting in an overall deteriorated pollution  
 598 scenario except for the north corner near Taipei. Notably, the sharp difference in PM<sub>2.5</sub>

599 enhancement indices between the areas surrounding Taipei and the adjacent western regions  
600 aligns with the configuration of local circulations, where the lee vortex circulation causes  
601 southwesterly winds in this area to shift to southeasterly winds. Consequently, pollutants from  
602 central and southern Taiwan cannot reach Taipei owing to the prevailing southeasterly local flow  
603 in the areas around Taipei originating in eastern Taiwan, where pollutant emission sites are  
604 scarce.

605 As the synoptic flow regime shifts from WD120 to WD150, the local flow pattern turns  
606 into an elongated anti-cyclonic circulation on the west plain of Taiwan (Fig. 7b). The curved  
607 southerly flow, which later shifts to westerly over northern Taiwan, provides an efficient  
608 pathway for transporting pollutants from central and southern Taiwan to the Taipei metropolitan  
609 area. Compared with the scenarios of WD120 shown in Fig. 7a, the weaker southeasterly in  
610 Taipei areas also promotes a favorable environment for the accumulation of pollutants.  
611 Meanwhile, the strong southerly in Kaohsiung can alleviate the locally emitted pollution,  
612 resulting in a distinct scenario of the pollution distribution under the WD150 flow regime.

613 In this study, we demonstrate that this reduced order model is an effective tool for  
614 evaluating local circulations that provides a reliable physical examination of the local pollution  
615 scenarios. The bifurcation of the pollution scenarios can be physically interpreted through the  
616 sharp transition of the local circulations caused by the synoptic flow regime shifting from  
617 WD120 to WD150.

618 The AI downscaling approach proposed in this study can be further applied to the climate  
619 projection scenarios to shed light on the prediction of the local response to changes in the large-  
620 scale circulation in the warming climate. While the CMIP6 models' output represents the most  
621 up-to-date climate modeling data for a better understanding of the future of the climate system  
622 given internal climate variability uncertainties, the horizontal resolution of the CMIP6 GCMs,  
623 which is usually over 100 km, is still too coarse to be used in adaptation management at local  
624 scale such as Taiwan. Leveraging the reduced-order model, we can obtain high-fidelity  
625 representations of local circulation patterns given the projected synoptic flow regime scenarios in  
626 the coarser CMIP6 simulations, while achieving significant computational savings compared to  
627 traditional dynamical downscaling approaches. To demonstrate the capability of this framework,  
628 an example is provided using the large-scale flow regime change in TaiESM1 model output as  
629 the synoptic controlling physical parameters to apply the reduced-order model. By projecting the  
630 occurrence difference on the latent space, we can clearly identify the synoptic flow regimes  
631 change and the corresponding local circulation responses, as shown in Fig. 8. The heatmap in the  
632 latent space displayed in Fig. 8a indicates that the weak (about  $4 \text{ m s}^{-1}$ ) easterly and the strong  
633 (about  $10 \text{ m s}^{-1}$ ) southerly flow regimes are more profoundly increased under the SSP585  
634 warming climate. By applying the reduced-order model to generate the local circulation based on  
635 these projected locations in the latent space, the local flow pattern can be evaluated as displayed  
636 in Fig. 8b and 8c. The local circulation response of the strong southerly scenario (Fig 8b)  
637 displayed a flow pattern akin to the scenario of the WD150 scenario (Fig. 7b) with an elongated  
638 anticyclonic circulation along the west coast of Taiwan that promotes the local pollutants  
639 transport from central and southern Taiwan to the Taipei metropolitan area. On the other hand,  
640 the weak easterly scenarios induces a dipole of the lee vortices on the west of Taiwan. The  
641 cyclonic flow of the northern vortex promotes strong southeasterly winds over the areas around  
642 Taipei, while the center of the southern vortex locates at Kaohsiung indicates that the weak wind  
643 situation in Kaohsiung city might favors the pollutants accumulation.



644  
 645 **Fig. 8 (a) The projected synoptic flow regimes change from current climate to SSP585**  
 646 **warming scenario in TaiESM1 in the latent space. Two most increased flow regimes are**  
 647 **selected to generate the corresponding local circulations indicating by the curved arrows as**  
 648 **(b) the local circulation under the strong southerly and (c) the local circulation under the**  
 649 **weak easterly. The correspondent synoptic wind speeds and directions are indicated in the**  
 650 **titles of subfigures (b) and (c). The synoptic flow regime change is defined as below: we**  
 651 **take the near-surface wind (at 1000 hPa) at the geographic location of Ishigaki island,**  
 652 **Japan, as the synoptic flow regime upstream to Taiwan in the cold season (Oct. to Apr.) for**  
 653 **a 20-year period in both of the historical (1990-2010) and SSP585 climate scenario(2079-**  
 654 **2099) experiment data. After confining the wind direction between 30° and 180°, and**  
 655 **excluding the sharp wind direction change around the nearby area of Taiwan as criteria**  
 656 **for filtering out the strong synoptic weather system such as the front system, the flow**  
 657 **regime change is calculated as the occurrence change of different flow regimes in these**  
 658 **filtered days between the current climate and SSP858 warming scenario.**  
 659

660  
 661 Examining the local circulation responses to the most possible increasing flow regimes  
 662 above indicates that the two major cities of Taiwan, namely Taipei and Kaohsiung, could  
 663 experience pollution deterioration from the local pollutant transport. The reduced-order model as  
 664 an AI downscaling tool provides an instantaneous evaluation of the high-resolution local  
 665 circulation given a specific synoptic flow regime. As a 48-hour semi-realistic simulation  
 666 conducted in this study takes 9 hours on a 64-core computer to create 132 snapshots of the local  
 667 circulations, it only takes 1.17 seconds for VAE to create the same local circulation ensembles.  
 668 While the physical model simulation can provide a comprehensive evolution of Taiwan's 3-  
 669 dimensional local circulation structure, we demonstrate that the reduced-order model can  
 670 accelerate the evaluation of the surface local circulation by more than 27,000 times. It shows this  
 671 framework's potential in assessing Taiwan's local circulation under multiple warming scenarios  
 672 or in the diverse CMIP GCM simulation results. Our ongoing work is to characterize the local  
 673 circulation response to East Asia's synoptic flow regime shift in CMIP6 multiple GCM members.  
 674 The diversity of the local response in the spread of the CMIP6 climate projection can be  
 675 examined through the reduced-order model. It is worth noting that this framework empowers the  
 676 efficiency of the VAE model prediction to the storyline approach of representing the uncertainty  
 in climate change proposed by Shephard et al. (2018). As the reduced-order model can

677 efficiently evaluate the local circulation, the uncertainty of the future local pollution events  
678 owing to the variability in the GCM projections can be isolated and evaluated. This advancement  
679 in modeling capabilities enables us to explore and understand the uncertainty of local weather  
680 phenomena in response to changing climate conditions with efficiency and accuracy. By utilizing  
681 this innovative approach, researchers can make more informed decisions regarding pollution  
682 control strategies and policy interventions to mitigate the environmental impacts of local  
683 pollution.

684 Furthermore, we emphasize that the explainable VAE framework introduced in this study  
685 has the potential to assess various weather regimes under climate change. With a clear physical  
686 connection established between synoptic controlling factors and specific local weather patterns, a  
687 series of ensemble LES experiments can be carried out focusing on the specific local weather  
688 regime that captures the various local responses to large-scale variability. By learning from this  
689 dataset, the reduced-order model of this specific weather regime can be constructed.

690

## 691 **Acknowledgments**

692 This study is supported jointly by Taiwan's NSTC through Grant 112-2111-M-002-015- and

693 Grant NTU112L7832 to National Taiwan University.

694

## 695 **Data Availability Statement**

696 All code used to produce figures, along with the VAE model, training and validation scripts, and  
697 reconstruction results are available for download here: <https://10.5281/zenodo.10086813>.

698 However, please note that due to file size limitations, we are unable to provide online access to  
699 the semi-realistic large ensemble simulations, the training dataset, and the TaiESM1 climate

700 data. If you require access to the training dataset, please contact the authors directly. The figures  
701 in this study were generated using Matplotlib version 3.5.1 (Hunter, 2007), which is available

702 under the Matplotlib license at <https://doi.org/10.5281/zenodo.5773480>.

703

## 704 **References**

705 Behrens, G., Beucler, T., Gentine, P., Iglesias-Suarez, F., Pritchard, M., & Eyring, V. (2022).

706 Non-Linear Dimensionality Reduction With a Variational Encoder Decoder to Understand

707 Convective Processes in Climate Models. *Journal of Advances in Modeling Earth Systems*,  
708 14(8), e2022MS003130. <https://doi.org/10.1029/2022MS003130>

709 Beucler, T., Gentine, P., Yuval, J., Gupta, A., Peng, L., Lin, J., et al. (2021, December 14).  
710 Climate-Invariant Machine Learning. arXiv. <https://doi.org/10.48550/arXiv.2112.08440>

711 Bhatia, S., Jain, A., & Hooi, B. (2021, March 15). ExGAN: Adversarial Generation of Extreme  
712 Samples. arXiv. <https://doi.org/10.48550/arXiv.2009.08454>

713 Bi, K., Xie, L., Zhang, H., Chen, X., Gu, X., & Tian, Q. (2023). Accurate medium-range global  
714 weather forecasting with 3D neural networks. *Nature*, 619(7970), 533–538.  
715 <https://doi.org/10.1038/s41586-023-06185-3>

716 Chang, Y.-H., Chen, W.-T., Wu, C.-M., Moseley, C., & Wu, C.-C. (2021). Tracking the  
717 influence of cloud condensation nuclei on summer diurnal precipitating systems over complex  
718 topography in Taiwan. *Atmospheric Chemistry and Physics*, 21(22), 16709–16725.  
719 <https://doi.org/10.5194/acp-21-16709-2021>

720 Chien, M.-H., & Wu, C.-M. (2016). Representation of topography by partial steps using the  
721 immersed boundary method in a vector vorticity equation model (VVM): VVM PARTIAL  
722 STEP. *Journal of Advances in Modeling Earth Systems*, 8(1), 212–223.  
723 <https://doi.org/10.1002/2015MS000514>

724 Daw, A., Karpatne, A., Watkins, W., Read, J., & Kumar, V. (2017, October 31). Physics-guided  
725 Neural Networks (PGNN): An Application in Lake Temperature Modeling. arXiv.  
726 <https://doi.org/10.48550/arXiv.1710.11431>

727 Eyring, V., Bony, S., Meehl, G. A., Senior, C. A., Stevens, B., Stouffer, R. J., & Taylor, K. E.  
728 (2016). Overview of the Coupled Model Intercomparison Project Phase 6 (CMIP6) experimental  
729 design and organization. *Geoscientific Model Development*, 9(5), 1937 - 1958.  
730 <https://doi.org/10.5194/gmd-9-1937-2016>

731 Goodfellow, I. J., Pouget-Abadie, J., Mirza, M., Xu, B., Warde-Farley, D., Ozair, S., et al.  
732 (2014). Generative Adversarial Networks. arXiv. <https://doi.org/10.48550/arXiv.1406.2661>

733 Hsieh, M.-K., Chen, Y.-W., Chen, Y.-C., & Wu, C.-M. (2022). The Roles of Local Circulation  
734 and Boundary Layer Development in Tracer Transport over Complex Topography in Central  
735 Taiwan. *Journal of the Meteorological Society of Japan. Ser. II*, 100(3), 555–573.  
736 <https://doi.org/10.2151/jmsj.2022-028>

- 737 Hsu, T.-H., Chen, W.-T., Wu, C.-M., & Hsieh, M.-K. (2023). The Observation-Based Index to  
738 Investigate the Role of the Lee Vortex in Enhancing Air Pollution over Northwestern Taiwan.  
739 *Journal of Applied Meteorology and Climatology*, 62(3), 427–439.  
740 <https://doi.org/10.1175/JAMC-D-22-0102.1>
- 741 Hunter, J. D. (2007). Matplotlib: A 2D Graphics Environment. *Computing in Science &*  
742 *Engineering*, 9(3), 90–95. <https://doi.org/10.1109/MCSE.2007.55>
- 743 Jung, J.-H., & Arakawa, A. (2008). A Three-Dimensional Anelastic Model Based on the  
744 Vorticity Equation. *Monthly Weather Review*, 136(1), 276–294.  
745 <https://doi.org/10.1175/2007MWR2095.1>
- 746 Karpatne, A., Atluri, G., Faghmous, J. H., Steinbach, M., Banerjee, A., Ganguly, A., et al.  
747 (2017). Theory-Guided Data Science: A New Paradigm for Scientific Discovery from Data.  
748 *IEEE Transactions on Knowledge and Data Engineering*, 29(10), 2318–2331.  
749 <https://doi.org/10.1109/TKDE.2017.2720168>
- 750 Kingma, D. P., & Welling, M. (2019). An Introduction to Variational Autoencoders. *Foundations*  
751 *and Trends® in Machine Learning*, 12(4), 307–392. <https://doi.org/10.1561/22000000056>
- 752 Kingma, D. P., & Welling, M. (2022, December 10). Auto-Encoding Variational Bayes. arXiv.  
753 Retrieved from <http://arxiv.org/abs/1312.6114>
- 754 Klemmer, K., Saha, S., Kahl, M., Xu, T., & Zhu, X. X. (2021, April 26). Generative modeling of  
755 spatio-temporal weather patterns with extreme event conditioning. arXiv.  
756 <https://doi.org/10.48550/arXiv.2104.12469>
- 757 Kuo, K.-T., & Wu, C.-M. (2019). The Precipitation Hotspots of Afternoon Thunderstorms over  
758 the Taipei Basin: Idealized Numerical Simulations. *Journal of the Meteorological Society of*  
759 *Japan. Ser. II*, 97(2), 501–517. <https://doi.org/10.2151/jmsj.2019-031>
- 760 Lai, H.-C., & Lin, M.-C. (2020). Characteristics of the upstream flow patterns during PM2.5  
761 pollution events over a complex island topography. *Atmospheric Environment*, 227, 117418.  
762 <https://doi.org/10.1016/j.atmosenv.2020.117418>
- 763 Lam, R., Sanchez-Gonzalez, A., Willson, M., Wirnsberger, P., Fortunato, M., Pritzel, A., et al.  
764 (2022, December 24). GraphCast: Learning skillful medium-range global weather forecasting.  
765 arXiv. <https://doi.org/10.48550/arXiv.2212.12794>

- 766 Lee, W.-L., Wang, Y.-C., Shiu, C.-J., Tsai, I. -chun, Tu, C.-Y., Lan, Y.-Y., et al. (2020). Taiwan  
767 Earth System Model Version 1: description and evaluation of mean state. *Geoscientific Model*  
768 *Development*, 13(9), 3887–3904. <https://doi.org/10.5194/gmd-13-3887-2020>
- 769 Lin, C.-Y., Sheng, Y.-F., Chen, W.-C., Chou, C. C. K., Chien, Y.-Y., & Chen, W.-M. (2021). Air  
770 quality deterioration episode associated with a typhoon over the complex topographic  
771 environment in central Taiwan. *Atmospheric Chemistry and Physics*, 21(22), 16893–16910.  
772 <https://doi.org/10.5194/acp-21-16893-2021>
- 773 Oliveira, D. A. B., Diaz, J. G., Zadrozny, B., & Watson, C. (2021, July 30). Controlling Weather  
774 Field Synthesis Using Variational Autoencoders. arXiv.  
775 <https://doi.org/10.48550/arXiv.2108.00048>
- 776 Pathak, J., Subramanian, S., Harrington, P., Raja, S., Chattopadhyay, A., Mardani, M., et al.  
777 (2022, February 22). FourCastNet: A Global Data-driven High-resolution Weather Model using  
778 Adaptive Fourier Neural Operators. arXiv. <https://doi.org/10.48550/arXiv.2202.11214>
- 779 Shamekh, S., Lamb, K. D., Huang, Y., & Gentine, P. (2022). Implicit learning of convective  
780 organization explains precipitation stochasticity (preprint). *Atmospheric Sciences*.  
781 <https://doi.org/10.1002/essoar.10512517.1>
- 782 Shen, Z., Sridhar, A., Tan, Z., Jaruga, A., & Schneider, T. (2022). A Library of Large-Eddy  
783 Simulations Forced by Global Climate Models. *Journal of Advances in Modeling Earth Systems*,  
784 14(3), e2021MS002631. <https://doi.org/10.1029/2021MS002631>
- 785 Shepherd, T. G., Boyd, E., Calel, R. A., Chapman, S. C., Dessai, S., Dima-West, I. M., et al.  
786 (2018). Storylines: an alternative approach to representing uncertainty in physical aspects of  
787 climate change. *Climatic Change*, 151(3), 555–571. <https://doi.org/10.1007/s10584-018-2317-9>
- 788 Wang, C., Tang, G., & Gentine, P. (2021). PrecipGAN: Merging Microwave and Infrared Data  
789 for Satellite Precipitation Estimation Using Generative Adversarial Network. *Geophysical*  
790 *Research Letters*, 48(5), e2020GL092032. <https://doi.org/10.1029/2020GL092032>
- 791 Wilby, R. L., & Dessai, S. (2010). Robust adaptation to climate change. *Weather*, 65(7), 180–  
792 185. <https://doi.org/10.1002/wea.543>
- 793 Wu, C.-M., & Arakawa, A. (2011). Inclusion of Surface Topography into the Vector Vorticity  
794 Equation Model (VVM): INCLUSION OF SURFACE TOPOGRAPHY INTO THE VVM.  
795 *Journal of Advances in Modeling Earth Systems*, 3(2), n/a-n/a.  
796 <https://doi.org/10.1029/2011MS000061>

797 Wu, C.-M., Lin, H.-C., Cheng, F.-Y., & Chien, M.-H. (2019). Implementation of the Land  
798 Surface Processes into a Vector Vorticity Equation Model (VVM) to Study its Impact on  
799 Afternoon Thunderstorms over Complex Topography in Taiwan. *Asia-Pacific Journal of*  
800 *Atmospheric Sciences*, 55(4), 701–717. <https://doi.org/10.1007/s13143-019-00116-x>  
801 Zadrozny, B., Watson, C. D., Szwarcman, D., Civitarese, D., Oliveira, D., Rodrigues, E., &  
802 Guevara, J. (2021, February 5). A modular framework for extreme weather generation. arXiv.  
803 <https://doi.org/10.48550/arXiv.2102.04534>